Biophysical Journal, Volume *117*

Supplemental Information

Voltage-Dependent Profile Structures of a Kv-Channel via Time-Resolved Neutron Interferometry

Andrey Y. Tronin, Lina J. Maciunas, Kimberly C. Grasty, Patrick J. Loll, Haile A. Ambaye, Andre A. Parizzi, Valeria Lauter, Andrew D. Geragotelis, J. Alfredo Freites, Douglas J. Tobias, and J. Kent Blasie

Supporting Material:

a) Analysis of the time-resolved neutron interferometry data:

The formalism describing the conventional x-ray or neutron reflectivity experiment was first developed for an amphiphilic macromolecule spread in a Langmuir monolayer at the liquid-gas (e.g., water-helium) interface (1), although it applies to the solid-gas and solid-liquid interfaces as well. Using monochromatic x-rays or neutrons, the reflectivity experiment involves recording the elastically reflected x-rays/neutrons as a function of the angle of incidence (α) which is maintained equal to the angle of reflection (β) for the case of specular reflectivity, both angles measured with respect to the plane of the interface. For the incident x-ray photon/neutron momentum vector $\overrightarrow{k_I}$ and reflected x-ray photon/neutron momentum vector $\overrightarrow{k_R}$, whose magnitudes are each $2\pi/\lambda$ for elastic scattering where λ is the photon/neutron wavelength, the photon/neutron momentum transfer vector for the scattering process is $\overrightarrow{Q_z} = (\overrightarrow{k_R} - \overrightarrow{k_I})$ which is parallel to the normal to the interface $\vec{z}$, where $|\overrightarrow{Q_z}| \equiv Q_z = (4\pi \sin\alpha)/\lambda$. Note that for specular x-ray/neutron reflectivity, $\overrightarrow{k_I}$, $\overrightarrow{k_R}$ and $\overrightarrow{Q_z}$ all lie in the same plane perpendicular to the interface. In this formalism, the Fresnel-normalized reflectivity $R(Q_z)/R_F(Q_z)$ is defined as the specular reflectivity $R(Q_z)$ divided by that from an ideal (flat and smooth) interface $R_F(Q_z)$ described by an analytic function. Furthermore, the Fresnel-normalized reflectivity $R(Q_z)/R_F(Q_z) = |F(Q_z')|^2$, where $F(Q_z') \equiv \frac{1}{\rho_{ave}} \int \frac{d\rho(z)}{dz} e^{iQ_z'z} dz$ and $(Q_z')^2 = \{(Q_z)^2 - sign(\rho_{ave})(Q_z)_{crit}^2\}$ with $(Q_z)_{crit}$ defined as Q_z at the critical angle for reflection. In this formalism developed in the Born approximation for elastic x-ray/neutron scattering, $F(Q_z')$ is proportional to the Fourier transform of the *gradient* of the scattering-length density profile $d\rho(z)/dz$. In general, $F(Q_z') = |F(Q_z')|e^{i\phi(Q_z')}$ where $|F(Q_z')|$ is the modulus and $\phi(Q_z')$ is the phase of the Fourier transform, the latter being lost upon recording the Fresnel-normalized reflectivity data $R(Q_z)/R_F(Q_z)$. This missing phase information must be recovered in order to unambiguously derive the *gradient* of the SLD profile $d\rho(z)/dz$ from the data, and hence the scattering-length density profile itself, $\rho(z)$, via integration. Note that in this formalism, with $F(Q_z')$ defined as the Fourier transform (FT) of the gradient SLD profile $d\rho(z)/dz$, then $d\rho(z)/dz$ is the inverse Fourier transform (FT^{-1}) of $F(Q_z')$, where both transforms are mathematically unique. Interferometry is a well-developed method for recovering this missing phase information that employs a so-called inorganic multilayer *reference* structure positioned sufficiently near the bio-organic ultrathin film, including immediately adjacent, for the interference effect to occur (2). Its application for the neutron case, using the above formalism, has been thoroughly documented in numerous references, beginning with reference (3). Our approach utilizes a constrained refinement to determine the unknown phase information, which is particularly well-suited to this formalism as described below. Briefly, $d\rho(z)/dz$ is of finite extent Δ, i.e., it is bounded, for an ultrathin bio-organic film with an adjacent inorganic multilayer at either the solid-liquid or the solid-gas interface because the SLD, $\rho(z)$, itself becomes constant for distances along the interface normal sufficiently far from the film. As a result, the autocorrelation of $d\rho(z)/dz$, namely $\left\{\frac{d\rho(z)}{dz} * \frac{d\rho(-z)}{dz}\right\}$, which can be obtained from the inverse Fourier transform of the data $R(Q_z)/R_F(Q_z) = |F(Q_z')|^2$ without any phase information, is similarly of finite extent 2Δ, possessing no information content for $|z| > \Delta$, thereby providing a key constraint on the to-be-derived gradient SLD profile. Since the SLD, $\rho(z)$, of the inorganic multilayer reference structure is essentially known from its fabrication

specifications, as can be confirmed by x-ray reflectivity in the absence of the adjacent bio-organic film, the phase of the Fourier transform of its gradient SLD profile $d\rho(z)/dz$ is also known by simple calculation. The constrained refinement is initiated, utilizing an inverse Fourier transform (FT^{-1}) of the experimental $|F(Q_z')|$ modulus data for the ultrathin bio-organic film adjacent the inorganic multilayer reference structure combined with the known phase of the reference structure's gradient SLD profile to calculate the first approximation to the gradient SLD profile for the ultrathin bio-organic film adjacent the inorganic multilayer reference structure. The key constraint is then applied by truncating this first approximation to the gradient SLD profile for $|z| > \Delta/2$ and a new phase function $\phi(Q_z')$ is created for the so-truncated gradient SLD profile via Fourier transformation (FT), which is then combined with the experimental $|F(Q_z')|$ modulus data for the ultrathin bio-organic film adjacent the inorganic multilayer reference structure to calculate the second approximation to the gradient SLD profile via inverse Fourier transformation (FT^{-1}). This process is then repeated until convergence is achieved, usually within less than 10 iterations. The converged gradient SLD profile $d\rho(z)/dz$ is then simply integrated to provide the SLD itself, $\rho(z)$.

There is a further consideration with regard to the formalism developed in reference (1), which is important to the "pump-probe" neutron interferometry approach described below. The reflectivity itself, $R(Q_z)$ decays over six to seven orders of magnitude with increasing momentum transfer Q_z (4). The Fresnel function $R_F(Q_z)$ is a precise analytic function, and hence division by the Fresnel function to result in the Fresnel-normalized reflectivity $R(Q_z)/R_F(Q_z)$ has no effect on the statistical accuracy inherent in the reflectivity data. However, the normalization does result in the Fresnel-normalized reflectivity being of comparable amplitude over the entire range of momentum transfer Q_z accessed in the experiment. Since the changes in the membrane nSLD profile $\rho(z)$, which are dependent on the applied transmembrane voltage, are expected to be relatively small due to the nature of the profile projection, the Fresnel normalization of the reflectivity data makes it much less difficult to readily ascertain whether the voltage-induced changes are statistically significant.

(b) Specimen-to-specimen reproducibility:

Four different KvAP-POPC membrane specimens were investigated that differed slightly in terms of the separation between the membrane and the surface of the SiGeSi multilayer substrate at the 1-2Å level, and the Fresnel-normalized neutron interferometry data, $R(Q_z)/R_F(Q_z)$, are exquisitely sensitive to this separation. Thus, it might appear that specimen-to-specimen reproducibility in terms of their dependence on the transmembrane voltage could only be ascertained from a complete analysis of the data through to the nSLD profiles for the membrane itself, which includes recovering the otherwise missing phase information, as opposed to a simple inspection of their respective $R(Q_z)/R_F(Q_z)$ data. However, the autocorrelation of $d\rho(z)/dz$, namely $\left\{\frac{d\rho(z)}{dz} * \frac{d\rho(-z)}{dz}\right\}$, can be obtained from the inverse Fourier transform of the data $R(Q_z)/R_F(Q_z) = |F(Q_z')|^2$ *without any phase information*, as described in section (a) above, and can thereby provide a different assessment as to whether the four specimens investigated exhibit any significant dependence on the transmembrane voltage. Figure SM 2 contains the autocorrelation functions calculated for the four specimens investigated S2-S5, along with that of the control specimen S1 comprised of only the Si-Ge-Si multilayer substrate and the organic self-assembled monolayer used to tether the KvAP channel protein to the surface of specimens S2-S5, all at a contrast provided by 90%D_2O/10%H_2O. As can be seen, the autocorrelation function

for S1 contains significant larger amplitude fluctuations only for $|z| < 100$Å, the smaller amplitude fluctuations for larger z-values arising from truncation of the inverse Fourier transform at the maximum value of Q_z accessed, namely ~ 0.2Å^{-1}. For specimens S2-S5, the autocorrelation functions contain significant larger amplitude fluctuations extending further out to $|z|$ ~ 200Å due to the presence of the KvAP-POPC membrane on their surface, and only smaller amplitude fluctuations for larger z-values arising from truncation of the inverse Fourier transform. Using for reference the minimal voltage dependence exhibited by specimen S1 lacking the KvAP-POPC membrane for $|z| < 200$Å, specimens S2 and S5 show a substantial dependence on the transmembrane voltage extending over the entire range for $|z| < 200$Å, and particularly in that region due to the presence of the membrane on the multilayer substrate's surface for 100Å < $|z|$ < 200Å. Specimens S3 and S4 show a distinctly smaller dependence on the transmembrane voltage over the entire range for $|z| < 200$Å, the voltage dependence essentially only appearing in that region due to the presence of the membrane on the multilayer substrate's surface nearer the boundary of the autocorrelation function, namely for ~ 140Å < $|z|$ < 200Å. On this basis, two of the four KvAP-POPC membrane specimens exhibit a substantial dependence on the transmembrane voltage while the other two exhibit a smaller dependence on the transmembrane voltage, but still not approaching that of the control specimen lacking the membrane. Not surprisingly in view of the above, like the $R(Q_z)/R_F(Q_z)$ data shown in Figure 3 for specimen S2, the $R(Q_z)/R_F(Q_z)$ data for specimen S5 also show experimentally significant differences in the mean of the $R(Q_z)/R_F(Q_z)$ data that exceed the standard errors consistently over small ranges of momentum transfer Q_z for both contrasts, becoming progressively more evident with increasing Q_z, and being somewhat larger for 60%D_2O/40%H_2O. On the other hand, while the $R(Q_z)/R_F(Q_z)$ data for specimens S3 and S4 do show differences in the mean of the $R(Q_z)/R_F(Q_z)$ data over small ranges of momentum transfer Q_z, these differences do not exceed the standard errors, i.e., the errors overlap. As a result of the above considerations of both the $R(Q_z)/R_F(Q_z)$ data and their respective inverse Fourier transforms, the autocorrelation functions, the dependence of both specimens S2 and S5 on the transmembrane voltage is clearly experimentally significant, while that for specimens S3 and S4 is more difficult to establish.

The *difference* ΔnSLD profiles at the two contrasts for the KvAP-POPC membrane of specimen S5 were entirely similar and of comparable amplitude to those shown in Figure 3 for specimen S2. Despite the difficulty in establishing the experimental significance of the dependence of specimens S3 and S4 on the transmembrane voltage noted at the end of the preceding paragraph, the changes in the *difference* ΔnSLD profiles for these two specimens were very similar to those for specimens S2 and S5, but smaller in amplitude by a factor of 2, thereby likely explaining the difficulty noted.

(c) Molecular dynamics simulations:

Kv1.2/2.1: For the Kv1.2/2.1 chimera channel embedded within a POPC bilayer, details of the long MD simulation trajectories in which both large depolarizing transmembrane voltages and subsequently large hyperpolarizing transmembrane voltages were applied to the membrane are provided in reference (5), and the corresponding Supplemental Information. With reference to Figure 1 in reference (5), the authors provided coordinates from "simulation 6" for the transmembrane domain of the Kv1.2/2.1 chimera channel, designated as Kv1.2/2.1-T1(-), sampled at intervals of 2.2 μs over the 220 μs trajectory. This sampling provided only six instantaneous configurations for the activated, open (depolarized) state of the channel from the

first 13.2 μs of the trajectory. For consistency, we selected only six instantaneous configurations over the last 13.2 μs of the trajectory for the deactivated, closed (hyperpolarized) state of the channel. For the membrane, the atom selection included the protein, water and lipid within the entire MD cell of dimensions 125Å x 125Å x 145Å. Each selected atom was binned into 0.5 Å steps along the transmembrane-axis for each of the sampled configurations. The neutron atomic scattering lengths were summed for each bin and these values were averaged over all 6 configurations to construct the time-averaged nSLD profile for each state of the Kv1.2/2.1 chimera channel. The origin was defined as the protein center of mass for each configuration. Different deuteration ratios were achieved by randomly selecting a fraction of the hydrogen atoms on water and polar hydrogens on the protein to replace with deuterium. The same approach was employed to calculate the separate time-averaged nSLD profiles for the protein, lipid and water components of the membrane as determined by the atom selection.

Kv1.2: Initial structures for the activated, open and deactivated, closed states of Kv1.2 were based on the models originally obtained via ROSETTA membrane protein structure prediction (6) and subsequently refined by molecular dynamics (MD) simulation in a hydrated POPC bilayer membrane environment coupled with experimental restraints (7). The cytoplasmic T1 domain was removed at residue 150 to provide just the transmembrane domain of the Kv1.2 channel, thereby including residues 151 to 421. Three of the crystallographic potassium ions from (8) in sites S1 and S3 of the selectivity filter and one in the internal vestibule were included in the simulations. The protein was solvated with POPC lipid molecules using the CHARMM-GUI (9), then placed in a water box of dimensions 120Åx120Åx100Å, and KCl was added to neutralize the system and set an ion concentration of 150 mM using the VMD Autoionize plugin. The final system had 140,889 atoms for the deactivated, closed state and 144,944 atoms for the activated, open state.

MD simulations were performed using NAMD software version 2.11 (10) with the CHARMM36 forcefield for the protein and lipids (11-14) and TIP3P waters (15). The simulations used a 2 fs timestep with a Langevin dynamics scheme for temperature control and the Nosé-Hoover Langevin piston for pressure control (16-17). Lengths of bonds involving hydrogen were fixed using the SHAKE (18) and SETTLE (19) algorithms. The smooth particle mesh Ewald method (20-21) was used to calculate electrostatic interactions with a cut-off at 11 Å, employing a switching function. Visualization and analysis of the trajectories were performed using VMD (22).

After 10,000 steps of minimization, the Kv1.2 systems were run in the NVT ensemble at 300 K for 2 ns with the protein held fixed. They were then run in the NPT ensemble at 300 K and 1 atm for 2 ns with harmonic restraints on the protein heavy atom positions using a force constant of 1.5 kcal/mol/Å^2. The protein restraints were removed over 1 ns. Both systems were then run in the NPT ensemble at 300 K and 1 atm for 55 ns. Harmonic restraints were placed on the three selectivity-filter potassium ions for the entire simulation with a force constant of 1 kcal/mol/Å^2.

We applied a depolarizing transmembrane voltage of 150 mV for the activated, open state and polarizing transmembrane voltage of -150 mV for the deactivated, closed state by applying a constant electric field along the transmembrane direction. Given the magnitudes of these voltage gradients and the very short lengths (55 ns) of the MD trajectories compared with those required to actually change the conformation of the Kv-channel (e.g., see reference (5)), the voltage gradients were only intended to help stabilize the respective states of the Kv-channel within the

hydrated bilayer membrane. The deactivated, closed state simulation had two additional restraints to ensure the pore remained closed. The first was a distance restraint between alpha-carbon atoms on residue 410 for opposing subunits. A harmonic potential, with a force constant of 5 kcal/mol/Å^2, was applied if the distance between the alpha-carbon atoms was greater than 11.5 Å. To maintain the alpha-helical secondary structure for the S6 helix, harmonic restraints with a force constant of 200 kcal/mol were applied to the helix backbone phi and psi dihedral angles. This was done using the Extrabonds feature in NAMD.

The last 50 ns of the trajectories for the activated, open and deactivated, closed states of Kv1.2 in the hydrated POPC bilayer were sampled at 100 ps intervals to generate 500 instantaneous configurations of the system used to calculate the time-averaged nSLD profiles. For the membrane, the atom selection included the protein, water and lipid within a cylinder of radius 50 Å extending outward from the center of the protein perpendicular to the transmembrane-axis. Each selected atom was binned into 0.5 Å steps along the transmembrane-axis for each of the sampled configurations. The neutron atomic scattering lengths were summed for each bin and these values were averaged over all 500 configurations to construct the time-averaged nSLD profile for each state of the Kv1.2 protein. The origin was defined as the protein center of mass for each configuration. Different deuteration ratios were achieved by randomly selecting a fraction of the hydrogen atoms on water and polar hydrogens on the protein to replace with deuterium. The same approach was employed to calculate the separate time-averaged nSLD profiles for the protein, lipid and water components of the membrane as determined by the atom selection.

KvAP: An improved model for the activated, open state of the KvAP protein within a hydrated POPC bilayer was constructed with respect to that in reference (23). The model was constructed by splicing the activated state of the VSDs, obtained from a 10μs MD simulation of the isolated VSD within a hydrated POPC bilayer at a depolarizing transmembrane voltage of 120mV (24-25) in which the S4 helix was in its outwardmost position, onto the presumed activated, open state of the pore domain (PD) obtained from a MD simulation of the complete homo-tetrameric KvAP within a hydrated POPC bilayer at a non-polarizing transmembrane voltage of 0mV (23). The VSD consisted of residues 24-147 and the PD contained residues 148-240. The splicing was accomplished by replacing the presumed activated VSDs (unpolarized) of the complete homo-tetrameric KvAP with the activated VSDs (depolarized) after aligning the Cα-atoms of only the S1 and S2 helices and then making minor manual adjustments to avoid overlap between the activated VSDs and the open PD. POPC lipids, waters, and ions were retained from the complete channel simulation (23). Following deletion of overlapping molecules, 50,000 steps of energy minimization were performed. The system dimensions were 165Åx165Åx100Å and contained 256,669 atoms in total: 13,832 protein atoms, 47,129 TIP3P waters, 755 POPC lipid molecules, 136 K^+ ions, and 144 Cl^- ions.

A MD simulation, otherwise similar to that described above for Kv1.2, was run in the NPT ensemble at 1 atm and 300 K with a depolarizing transmembrane voltage of 150mV to help stabilize the activated state of the VSDs. The protein heavy atoms were held fixed for 6 ns, followed by harmonic restraints on atom positions using a force constant of 10 kcal/mol/Å^2 for 8 ns, followed by harmonic restraints on just the protein backbone atom positions with a force constant of 1 kcal/mol/Å^2 for 20 ns. The last 10 ns of this restrained trajectory was sampled at 20ps intervals to generate 500 instantaneous configurations of the system used to calculate the time-averaged nSLD profiles. Note that the activated (depolarized) state of the VSD in the

simulation in reference (24) was stable over the last 5μs of the 10μs trajectory following application of the depolarizing transmembrane voltage. Thus, despite the short length of the restrained trajectory, this sampling was deemed sufficient because its primary purpose was to allow for the relaxation of the lipid and water molecules in response to embedding this activated, open (depolarized) state of the KvAP protein in the POPC bilayer.

The structure for the deactivated, closed state of KvAP was taken directly from the targeted MD simulation of reference (23). Following removal of the targeting restraints used to induce this state, the trajectory was continued unrestrained under a polarizing transmembrane voltage of -100mV for 280ns. The unrestrained trajectory was sampled at 5ns sampling intervals to generate 56 instantaneous configurations of the system used to calculate the time-averaged nSLD profiles.

For both the activated, open (depolarized) and deactivated, closed (polarized) states of the KvAP protein in the hydrated POPC bilayer, the atom selection for the nSLD profiles included the protein, water and lipid within a cylinder of radius 44 Å extending outward from the center of the protein perpendicular to the transmembrane-axis. This selection yielded a molar ratio of about 130 POPC:1 KvAP, approximately that for the experimental KvAP-POPC membrane. Each selected atom was binned into 0.5 Å steps along the transmembrane-axis for each of the sampled configurations. The neutron atomic scattering-lengths were summed for each bin and these values were averaged over all of the sampled configurations to construct the time-averaged nSLD profile for each state of the KvAP protein. The origin was defined as the protein center of mass for each sampled configuration. Different deuteration ratios were achieved by randomly selecting a fraction of the hydrogen atoms on water and polar hydrogens on the protein to replace with deuterium. The same approach was employed to calculate the separate time-averaged nSLD profiles for the protein, lipid and water components of the membrane as determined by the atom selection.

(d) Effect of the spatial resolution on detecting smaller translations of the S4 helix:

With respect to the three main features in the experimental *difference* ΔnSLD profile (hyperpolarized - depolarized) at a contrast of 60%D_2O in Figure 7A, the larger maximum occurs near the cytoplasmic surface of the membrane separated from a second maximum within the cytoplasmic half of the membrane by 28Å while the minimum occurs within the extracellular half of the membrane separated from the first maximum by 50Å. The two separations of these three main features are the only unique attributes of the experimental ΔnSLD profile. The experimental nSLD profile for the KvAP-POPC membrane is dominated by the KvAP protein. As a result, it is notable that the ΔnSLD profiles for both the simulated Kv1.2/2.1 chimera protein and the simulated Kv1.2 protein within their respective POPC bilayer membranes exhibit the same three features, namely two maxima and one minimum that span their respective membrane profiles. From Table 1 in the main manuscript, the two unique separations for the ΔnSLD profile of the Kv1.2/2.1 chimera protein match those of the experimental KvAP-POPC membrane to within less than 1Å. However, the two unique separations for the ΔnSLD profile of the Kv1.2 protein are 6-8Å smaller than those for the experimental KvAP-POPC membrane. Hence, the question arises as to whether our time-resolved neutron interferometry experiments could have detected these smaller separations given the relatively low spatial-resolution of the experimental nSLD profiles for the KvAP-POPC membrane at hyperpolarizing and depolarizing transmembrane voltages.

To address this important issue, slab models (4) were generated for the nSLD profiles of the experimental KvAP-POPC membrane, based on a finite sum of error functions and designated as Model 1 in Figure SM 4A. Least-squares fitting was employed to match the features of the experimental nSLD profiles for the membrane at both a depolarizing transmembrane voltage of -20mV and a hyperpolarizing voltage of +150mV, as well as the features of the modulus square of the Fourier transform of the gradient nSLD profiles, the experimental Fresnel-normalized neutron reflectivity. The *difference* ΔnSLD profile (hyperpolarized - depolarized) for the slab models is shown in Figure SM 4C. The corresponding resolution-limited nSLD profile for Model 1 in Figure SM 4B was calculated via Fourier transformation of its gradient nSLD profile into momentum transfer space (Q_z), followed by inverse Fourier transformation back into real space (z) at the experimental resolution defined by the maximum value of Q_z to which the experimental Fresnel-normalized neutron reflectivity was observed. This was followed by integration to produce the resolution-limited nSLD profiles. The difference (hyperpolarized - depolarized) of these resolution-limited profiles produced the ΔnSLD profile shown in the Figure SM 4D. Since the largest feature in the experimental ΔnSLD profile occurs near the cytoplasmic surface of the membrane, we decided to investigate the effect of the experimental spatial resolution on our ability to detect translations of the cytoplasmic interface in Model 1 toward the centroid of the membrane nSLD profile, while maintaining all other features constant. Two additional slab models were generated in which the translation was 8Å for Model 2 and 12Å for Model 3. The resolution-limited nSLD profiles were calculated for Models 2 and 3 as described above for Model 1, followed by calculation of the corresponding difference ΔnSLD profiles shown in the Figure SM 4E. As evident in Figure SM 4E, the first maximum near the cytoplasmic surface remains distinguishable from the second maximum for both Model 2 and Model 3 at the experimental spatial-resolution. From the parameter Table in Figure SM 4, the two unique parameters for the ΔnSLD profile of Model 2 are 2Å larger than for the ΔnSLD profile of the Kv1.2 protein while those for the ΔnSLD profile of Model 3 are 1-2Å smaller than those for the Kv1.2 protein. Thus, it appears that a translation of the cytoplasmic interface by ~10Å would have matched the parameters for the ΔnSLD profile for the Kv1.2 protein, while no translation represented by the ΔnSLD profile for Model 1 matches the parameters for both the Kv1.2/2.1 chimera protein and the KvAP protein. The ΔnSLD profiles for both the Kv1.2/2.1 protein and the Kv1.2 protein are dominated by the VSDs throughout the membrane profile, although the PD also makes a contribution near the cytoplasmic surface of the membrane, as shown for the Kv1.2/2.1 chimera protein in Figure SM 3. Thus, the smaller translation of ~7Å for the S4-helix within the VSDs of Kv1.2 would have indeed been distinguishable from the larger translation of ~15Å for the S4-helix within the VSDs for Kv1.2/2.1, given the experimental spatial-resolution of the nSLD profiles for the KvAP-POPC membrane (hyperpolarized and depolarized).

Supporting Material References:

(1) Als-Nielsen, J., D. Jacquemain, K. Kjaer, F. Leveiller, M. Lahav, and L. Leiserowitz. 1994. Principles and applications of grazing incidence x-ray and neutron scattering from ordered molecular monolayers at the air-water interface. Phys. Rep. 246:251-313.

(2) Krishnan, V., J. Strzalka, J. Liu, C. Liu, I. Kuzmenko, T. Gog, and J.K. Blasie. 2010. Interferometric enhancement of x-ray reflectivity from unperturbed Langmuir monolayers of amphiphiles at the liquid-gas interface. Phys. Rev. E 81:021604-1-10.

(3) Kneller, L.R., A.M. Edwards, C.F. Majkrzak, N.F. Berk, S. Krueger, and J.K. Blasie. 2001. Hydration state of a single cytochrome c monolayer vectorially-oriented at a soft interface investigated via neutron interferometry. Biophys. J. 80(5):2248-2261.

(4) Gupta, S., J. Dura, A. Freites, D. Tobias, and J.K. Blasie. 2012. Structural characterization of the voltage sensor domain and voltage-gated K^+-channel proteins vectorially-oriented within a single bilayer membrane at the solid/vapor and solid/liquid interfaces *via* neutron interferometry. Langmuir 28(28):10504-10520.

(5) Jensen, M.Ø., V. Jogini, D.W. Borhani, A.E. Leffler, R.O. Dror, and D.E. Shaw. 2012. Mechanism of voltage gating in potassium channels. Science 336:229-233.

(6) Yarov-Yarovoy, V., D. Baker, and W.A. Catterall. 2006. Voltage sensor conformations in the open and closed states in *ROSETTA* structural models of K^+ channels. Proc. Nat. Acad. Sci. USA. 103(19):7292-7297.

(7) Pathak, M.M., V. Yarov-Yarovoy, G. Agarwal, B. Roux, P. Barth, S. Kohout, F. Tombola, and E.Y. Isacoff. 2007. Closing in on the resting state of the Shaker K^+ channel. Neuron. 56:124-140.

(8) Long, S.B., E.B. Campbell, and R. MacKinnon. 2005. Crystal structure of a mammalian voltage-dependent *Shaker* family K^+ channel. Science. 309:897-903.

(9) Jo, S., T. Kim, V.G. Iyer, and W. Im. 2008. CHARMM-GUI: a web-based graphical user interface for CHARMM. J. Comput. Chem. 29:1859-1865.

(10) Phillips, J.C., R. Braun, W. Wang, J. Gumbart, E. Tajkhorshid, E. Villa, C. Chipot, R.D. Skeel, L. Kalé, and K. Schulten. 2005. Scalable molecular dynamics with NAMD. J. Comput. Chem. 26:1781-1802.

(11) MacKerell, Jr., A.D., D. Bashford, M. Bellott, R.L. Dunbrack, J.D. Evanseck, M.J. Field, S. Fischer, J. Gao, H. Guo, S. Ha, D. Joseph-McCarthy, L. Kuchnir, K. Kuczera, F.T. Lau, C. Mattos, S. Michnick, T. Ngo, D.T. Nguyen, B. Prodhom, W.E. Reiher, B. Roux, M. Schlenkrich, J.C. Smith, R. Stote, J. Straub, M. Watanabe, J. Wiórkiewicz-Kuczera, D. Yin, and M. Karplus. 1998. All-atom empirical potential for molecular modeling and dynamics studies of proteins. J. Phys. Chem. B. 102:3586-3616.

(12) MacKerell, Jr., A.D., M. Feig, and C.L. Brooks, III. 2004. Extending the treatment of backbone energetics in protein force fields: limitations of gas-phase quantum mechanics in reproducing protein conformational distributions in molecular dynamics simulations. J. Comput. Chem. 25: 1400-1415.

(13) Best, R.B., X. Zhu, J. Shim, P.E.M. Lopes, J. Mittal, M. Feig, and A.D. MacKerell Jr. 2012. Optimization of the additive CHARMM all-atom protein force field targeting improved sampling of the backbone phi, psi and side-chain chi1 and chi2 dihedral angles. J. Chem. Theory Comput. 8:3257-3273.

(14) Klauda, J.B., R.M. Venable, J.A. Freites, J.W. O'Connor, D.J. Tobias, C. Mondragon-Ramirez, I. Vorobyov, A.D. MacKerell Jr., and R.W. Pastor. 2010. Update of the CHARMM all-atom additive force field for lipids: validation on six lipid types. J. Phys. Chem. B. 114:7830–7843.

(15) Jorgensen, W.L., J. Chandrasekhar, J.D. Madura, R.W. Impey, and M.L. Klein. 1983. Comparison of simple potential functions for simulating liquid water. J. Chem. Phys. 79:926–935.

(16) Martyna, G.J., D.J. Tobias, and M.L. Klein. 1994. Constant-pressure molecular-dynamics algorithms. J. Chem. Phys. 101:4177-4189.

(17) Feller, S.E., Y. Zhang, R.W. Pastor, and B.R. Brooks. 1995. Constant pressure molecular dynamics simulation: the Langevin piston method. J. Chem. Phys. 103:4613-4621.

(18) Ryckaert, J.-P., G. Ciccotti, and H.J.C. Berendsen. 1977. Numerical integration of the Cartesian equations of motion of a system with constraints: molecular dynamics of n-alkanes. J. Comput. Phys. 23:327-341.

(19) Miyamoto, S., and P. Kollman. 1992. An analytical version of the SHAKE and RATTLE algorithm for rigid water models. J. Comput. Chem. 13:952-962.

(20) Essmann, U., L. Perera, M.L. Berkowitz, T. Darden, H. Lee, and L.G. Pedersen. 1995. A smooth particle mesh Ewald method. J. Chem. Phys. 103:8577–8593.

(21) Darden, T., D. York, and L. Pedersen. 1993. Particle mesh Ewald: an $N\cdot\log(N)$ method for Ewald sums in large systems. J. Chem. Phys. 98:10089-10092.

(22) Humphrey, W., A. Dalke, and K. Schulten. 1996. VMD: visual molecular dynamics. J. Mol. Graph. 14:33-38, 27-28.

(23) Schow, E.V., J.A. Freites, A. Nizkorodov, S.H. White, D.J. Tobias. 2012. Coupling between the voltage-sensing and pore domains in a voltage-gated potassium channel. Biochim. Biophys. Acta. 1818:1726-1736.

(24) Freites, J.A., E.V. Schow, S.H. White, and D.J. Tobias. 2012. Microscopic Origin of Gating Current Fluctuations in a Potassium Channel Voltage Sensor. Biophys. J. 102:L44-L46.

(25) Tronin, A., J.W. Strzalka, I. Kuzmenko, D. Worcester, V. Lauter, J.A. Freites, D.J. Tobias, and J.K. Blasie. 2014. Direct evidence of conformational changes associated with voltage-gating in a voltage sensor protein by time-resolved x-ray/neutron interferometry. Langmuir 30(16):4784-4796.

Supporting Material Figure Legends:

Figure SM 1: Typical Electrical Impedance Spectroscopy (EIS) data shown as Nyquist plots.
(A) The SAM (circles) on a monolayer graphene on Si-Ge-Si substrate.
(B) The KvAP-POPC membrane (circles) on the same monolayer graphene on Si-Ge-Si substrate.
(C) The KvAP-POPC membrane (circles) on a Si-Ge-Si substrate.
The best model fits to the respective EIS data (red) utilized one R-RC circuit to represent the substrate and a second RC circuit in series to represent the bio-organic overlayer on its surface. The EIS data were acquired using a CHI660D Electrochemical Workstation (CH Instruments). The electrochemical cell was either that used in the time-resolved neutron interferometry experiments or a similar cell to accommodate the smaller area (e.g., 1 x 2cm^2) of the substrates employed in the x-ray interferometry experiments.

Figure SM 2: Autocorrelation functions $\left\{\frac{d\rho(z)}{dz} * \frac{d\rho(-z)}{dz}\right\}$.
The autocorrelation functions for the hyperpolarizing transmembrane voltage are shown in blue and those for the depolarizing voltage are shown in red. For clarity, the ordinate and abscissa are labeled only for the specimen S1 SAM in Panel (E).
(A) Specimen S2 KvAP:POPC membrane at a contrast of 90% D_2O/10% H_2O.
(B) Specimen S5 KvAP:POPC membrane at a contrast of 90% D_2O/10% H_2O.
(C) Specimen S4 KvAP:POPC membrane at a contrast of 90% D_2O/10% H_2O.
(D) Specimen S3 KvAP:POPC membrane at a contrast of 90% D_2O/10% H_2O.
(E) Specimen S1 SAM at a contrast of 90% D_2O/10% H_2O.

Figure SM 3: Decomposition of the ΔnSLD(z) profile (hyperpolarized – depolarized) for the transmembrane domain of the Kv1.2/2.1 chimera.
(Blue)- ΔnSLD(z) profile for the transmembrane domain of the Kv1.2/2.1 protein within a hydrated POPC bilayer from Figure 7.
(Green)- ΔnSLD(z) profile for only the VSDs within the transmembrane domain of the Kv1.2/2.1 protein.
(Red)- ΔnSLD(z) profile for only the PD within the transmembrane domain of the Kv1.2/2.1 protein.

Figure SM 4: Modeling the three main features in the *difference* ΔnSLD profile (hyperpolarized – depolarized) for KvAP.
(A) Slab model (Model 1) profiles for the nSLD(z) profiles of the experimental KvAP-POPC membrane at a contrast of 60% D_2O/40% H_2O (hyperpolarized, blue; depolarized, red).
(B) Resolution-limited nSLD(z) profiles calculated for the Model 1 profiles in (A) at the spatial-resolution of the experiment.
(C) The *difference* ΔnSLD(z) profile (hyperpolarized-depolarized) for the slab model (Model 1) profiles in (A).
(D) The *difference* ΔnSLD(z) profile (hyperpolarized-depolarized) for the resolution-limited nSLD(z) profiles in (B).
(E) Comparison of the resolution-limited ΔnSLD(z) profiles for slab Model 1 (black) with those for slab models in which the cytoplasmic interface in panel (A) is shifted by 8Å (Model 2,

magenta) or 12Å (Model 3, turquoise) toward the centroid of the membrane nSLD profile at ~75Å.

(Table) The two unique separations of the three main features in ΔnSLD profiles are compared for the KvAP protein within the experimental KvAP-POPC membrane, for the Kv1.2/2.1 chimera protein within the simulated Kv1.2/2.1-POPC membrane, for the Kv1.2 protein within the simulated Kv1.2-POPC membrane, and for the resolution-limited Models 1-3.

Figure SM 1:

(A) SAM on Graphene

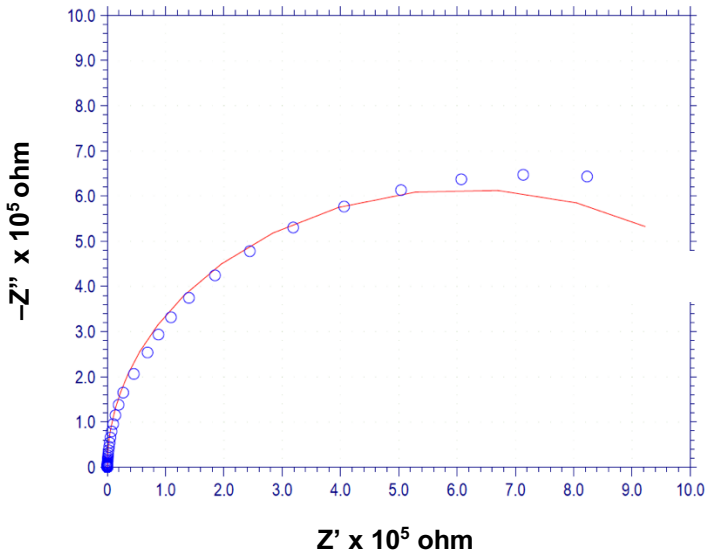

(B) KvAP-POPC on Graphene

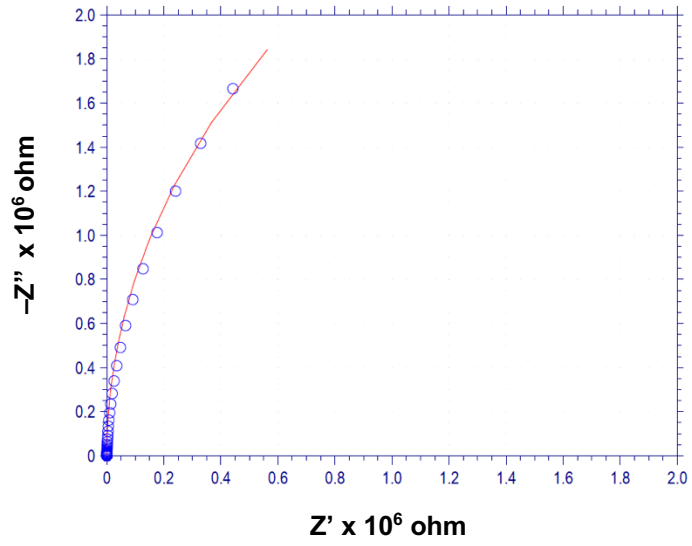

(B) KvAP-POPC on Silicon

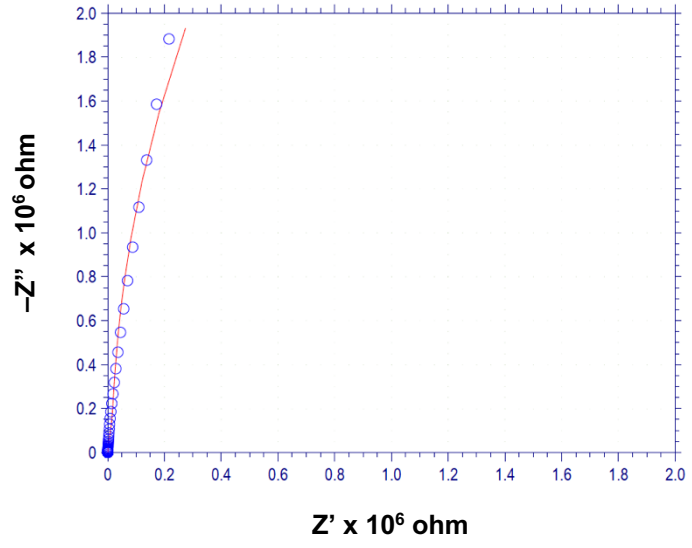

Figure SM 2:

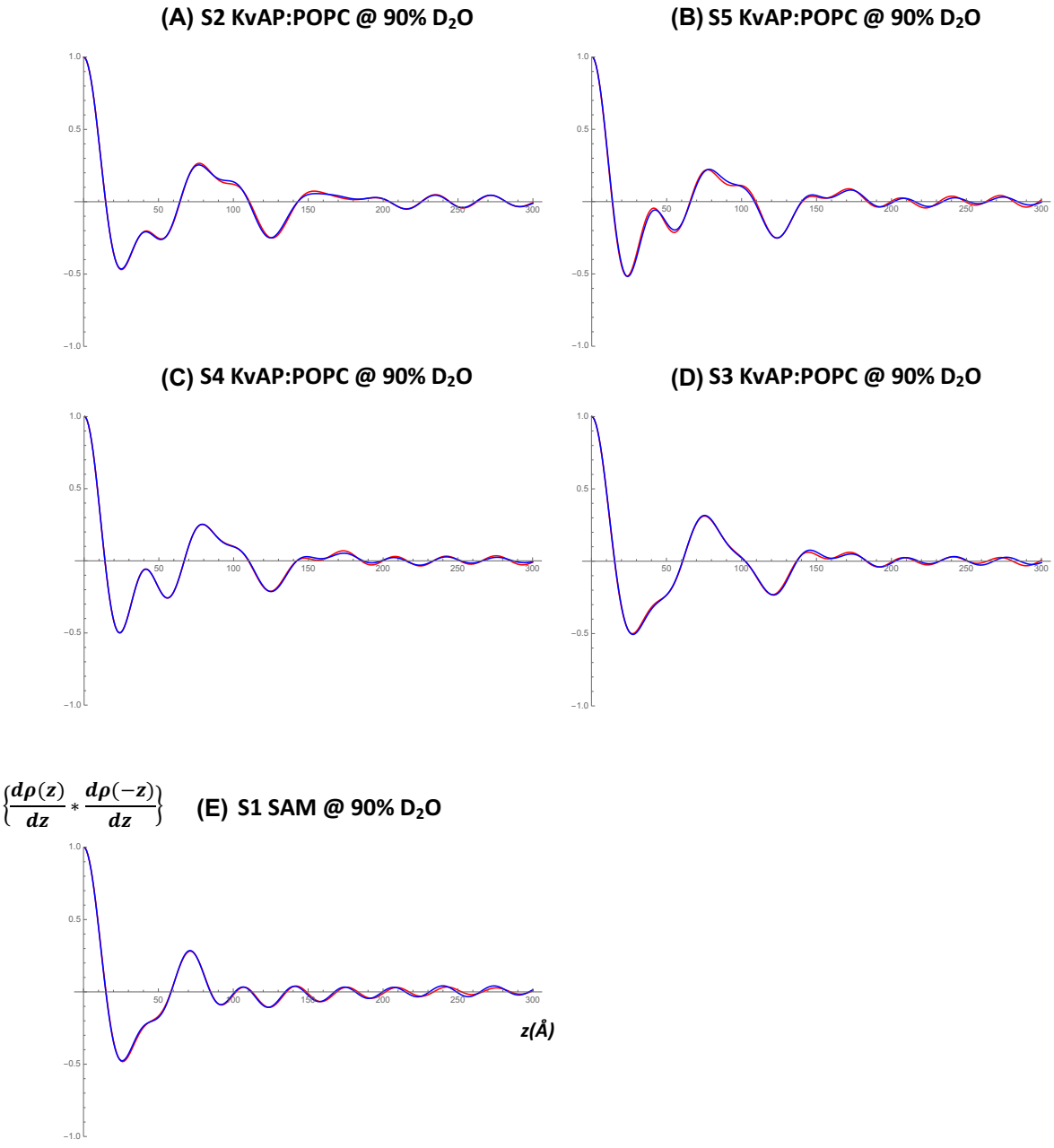
(A) S2 KvAP:POPC @ 90% D2O
(B) S5 KvAP:POPC @ 90% D2O
(C) S4 KvAP:POPC @ 90% D2O
(D) S3 KvAP:POPC @ 90% D2O
$\left\{\frac{d\rho(z)}{dz} * \frac{d\rho(-z)}{dz}\right\}$
(E) S1 SAM @ 90% D2O
z(Å)

Figure SM 3:

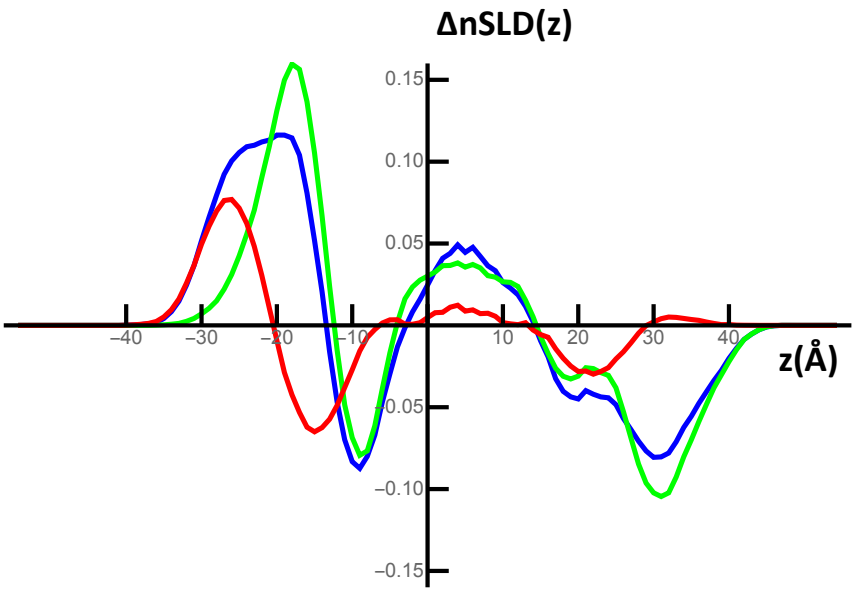

Figure SM 4:

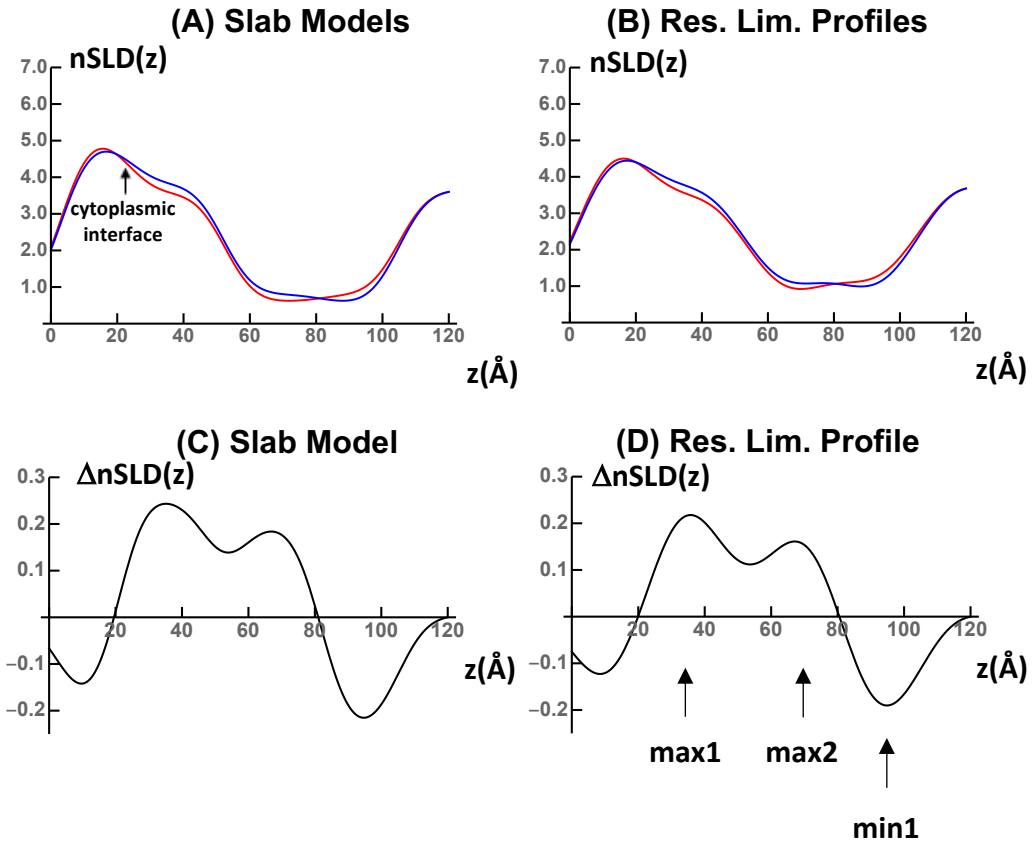

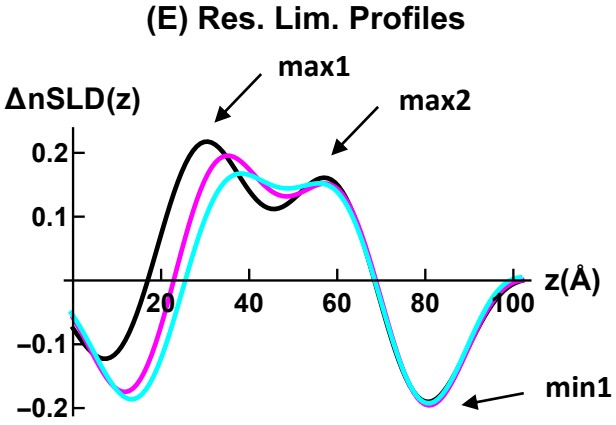

	Exp ΔnSLD KvAP	ΔnSLD Kv1.2/2.1	ΔnSLD Kv1.2	Resolution-limited ΔnSLD model 1	Resolution-limited ΔnSLD model 2	Resolution-limited ΔnSLD model 3
|Δ(max1-max2)|	28Å	28Å	20Å	27Å	22Å	18Å
|Δ(max1-min1)|	50Å	51Å	44Å	50Å	46Å	43Å